ChemComm

ROYAL SOCIETY OF CHEMISTRY

COMMUNICATION

View Article Online
View Journal | View Issue

Cite this: *Chem. Commun.*, 2024, **60**, 6941

Received 18th April 2024,
Accepted 10th June 2024

DOI: 10.1039/d4cc01834f

rsc.li/chemcomm

Ni_2P active site ensembles tune electrocatalytic nitrate reduction selectivity†

Emily Nishiwaki,[a] Peter S. Rice,[b] Ding-Yuan Kuo,[a] Florence Y. Dou,[a] Anthony Pyka,[c] Bryce Reid,[c] Hao A. Nguyen,[a] Eric M. Stuve,[c] Simone Raugei[b] and Brandi M. Cossairt*[a]

We demonstrate that active site ensembles on transition metal phosphides tune the selectivity of the nitrate reduction reaction. Using Ni_2P nanocrystals as a case study, we report a mechanism involving competitive co-adsorption of H* and NO_x* intermediates. A near 100% faradaic efficiency for nitrate reduction over hydrogen evolution is observed at −0.4 V, while NH_3 selectivity is maximized at −0.2 V *vs.* RHE.

Ammonia is an essential fertilizer for supporting global food demands.[1] It is produced industrially *via* the Haber–Bosch process, which combines gaseous nitrogen and hydrogen at high temperatures and pressures over an iron-based heterogeneous catalyst. However, the enormous scale of ammonia production and deployment has disrupted the nitrogen cycle, where imbalances of NO_3^- in wastewater and extraneous nitrous oxides emitted into the atmosphere from burning fossil fuels for H_2 production have resulted in ecosystem destruction and climate change.[2,3] Anthropogenic disturbances to the nitrogen cycle motivate alternative ammonia generation methods that do not exacerbate these imbalances. One alternative is the electrocatalytic nitrate reduction reaction (NO_3RR), which can upcycle NO_3^- to NH_3.[4] State-of-the-art catalysts usually include noble metals,[5–9] but current electrocatalyst design research focuses on using earth-abundant metals to achieve similar current densities.[10–13]

Several studies have proposed a NO_3RR mechanism that involves the co-adsorption of hydrogen (H*) and nitrogenous species (NO_x*) and sequential deoxygenation-hydrogenation to convert NO_3^- to NH_3.[14–16] With this knowledge, metal phosphides have been designed and demonstrated as selective NO_3RR electrocatalysts toward NH_3.[17–25] We hypothesize that metal phosphides have active site ensembles of adjacent strongly and weakly H-binding sites.[26] On these surfaces, strongly bound H can hydrogenate NO_x*, which can bind on a vacated site that only weakly adsorbs hydrogen.[27] Density functional theory (DFT) calculations have suggested that active site ensembles of strongly and weakly binding hydrogen sites are responsible for Ni_2P's HER activity.[28–32] The importance of these ensembles has also been realized in more complex electrocatalytic reactions such as CO_2 electroreduction, where several metal phosphides have demonstrated the ability to form oxygenated hydrocarbons.[33–37] The binary surfaces of metal phosphides result in an increased number of unique surface sites and a distribution of adsorbate-binding energetics, which enhance their ability to co-adsorb different species.

Thermal hydrogenation studies with Ni_2P and Ni nanocrystals showed Ni_2P's near unity selectivity toward NH_3 under mild conditions, while Ni had almost no conversion of NO_3^-.[38] This confirms the importance of a multi-elemental catalyst and motivates the investigation of nickel phosphide materials as electrocatalysts for NO_3RR. Although previous theoretical work on Ni_2P electrocatalysts for NO_3RR has highlighted the critical role of Ni_2P's ability to co-adsorb NO_3^- and H,[20,24] corroborating experimental data has not yet been reported. In this study, we investigate the nitrate reduction behavior of Ni_2P nanocrystals as a case study for elucidating the role of metal phosphide active site ensembles on NO_3^- reduction behavior. Our rate order analysis suggests a competitive Langmuir–Hinshelwood mechanism, which we use to understand the selectivity of Ni_2P for nitrate reduction over a range of reductive potentials.

Ni_2P nanocrystals were prepared according to previous methods developed in our group.[39] Briefly, $NiCl_2$ was added to oleylamine and degassed at 120 °C for 1 hour. The temperature was lowered to 50 °C, tris(diethylamino) phosphine was injected, and the temperature was raised to 250 °C and held for 1 hour. X-ray diffraction (XRD) and transmission electron microscopy (TEM) measurements show monodisperse, 5.4 ± 0.8 nm nanocrystals (Fig. S3, ESI†). Ni_2P nanocrystals were deposited onto Vulcan carbon (Ni_2P/C) to prevent aggregation

[a] Department of Chemistry, University of Washington, Seattle, WA 98195, USA. E-mail: cossairt@uw.edu
[b] Pacific Northwest National Laboratory, Richland, Washington, WA 99352, USA
[c] Department of Chemical Engineering, University of Washington, Seattle, WA 98195, USA

† Electronic supplementary information (ESI) available: Experimental and computational methods, supplementary data, acknowledgements. See DOI: https://doi.org/10.1039/d4cc01834f

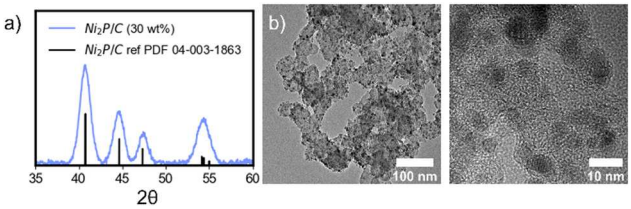

Fig. 1 (a) XRD and (b) TEM images of Ni_2P nanocrystals deposited on Vulcan carbon and annealed (Ni_2P/C).

during annealing with slight modifications from previous methods (see ESI†).[40] The nanocrystals were kept under inert conditions at all times to prevent surface oxidation before electrocatalytic measurements. XRD and TEM measurements of Ni_2P/C demonstrate the retention of the Ni_2P crystal structure post-annealing with mild ripening to 5.8 ± 1.5 nm (Fig. 1). Fourier transform analysis of the particle lattice fringes reveals predominantly (111)-faceted nanocrystals after the annealing treatment (Fig. S6, ESI†). The Ni_2P/C powder was drop-cast onto carbon paper electrodes (0.09 mg of Ni_2P) for electrocatalytic measurements (Fig. S5, ESI†). All electrochemical measurements were performed in an H-cell with a 0.1 M phosphate buffer electrolyte (1 : 1 KH_2PO_4/K_2HPO_4, pH = 6.9).

We performed cyclic voltammetry using Ni_2P/C with varying concentrations of KNO_3 to demonstrate Ni_2P/C's activity for NO_3RR (Fig. 2a). We attribute the two features to the catalytic activity being mediated by two different sources: H_2PO_4 and H_2O. With 0 mM KNO_3, we can isolate the catalytic activity to the HER. Under these conditions, HER activity first exhibits a diffusion-limited response near −0.3 V due to the H-source being $H_2PO_4^-$ ($pK_{aH_2PO_4^-} < pK_{aH_2O}$). As the potential increases and the water dissociation potential is reached, the HER current resembles the expected catalytic wave, indicating that

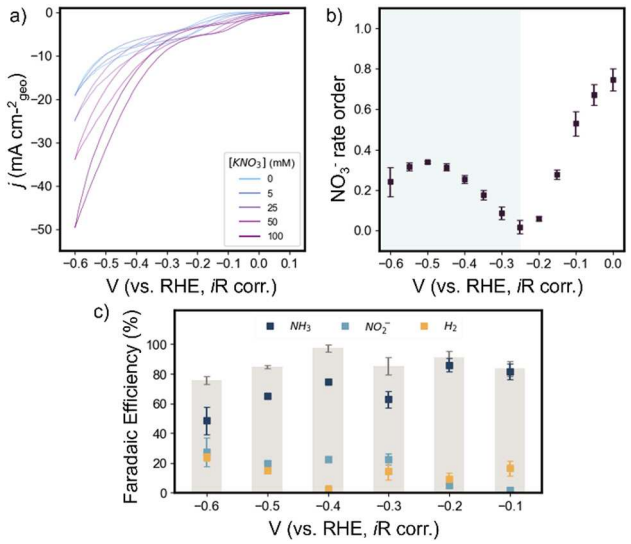

Fig. 2 (a) Cyclic voltammograms of Ni_2P/C in 0.1 M KH_2PO_4/K_2HPO_4 buffer at a series of KNO_3 concentrations. (b) Potential-dependent NO_3^- rate order. The region highlighted in blue (<−0.25 V) indicates a competitive Langmuir–Hinshelwood mechanism. (c) Potential-dependent selectivity with 100 mM of KNO_3.

the H-source is H_2O.[41] As the concentration of KNO_3 is increased, we observe diffusion-limited NO_3RR at low cathodic potentials in the phosphate-mediated region. In both regions, there is a decrease in onset potential and an increase in current density associated with an increased concentration of KNO_3, demonstrating Ni_2P/C's activity for NO_3RR.

Varying the concentration of KNO_3 allows for determining the nitrate rate order over a range of potentials, which provides insight into the adsorbate dynamics on the catalyst surface (Fig. 2b).[41] The NO_3^- rate orders were extracted from the logarithmic relationship between the current and the concentration of KNO_3 at a given potential (Fig. S9, ESI†). In the H_2O-mediated region (<−0.25 V, highlighted in blue in Fig. 2b), we observe an inverted-parabolic shape, which suggests that NO_3RR is proceeding *via* a Langmuir–Hinshelwood mechanism,[41,42] where H* and NO_x* are co-adsorbed, and the coverage ratio between the two dictates selectivity between NO_3RR and HER. This conclusion assumes that the rate-limiting step is the reduction of NO_3* to NO_2*, which has been proposed in previous studies.[14,43] The potential of maximum rate order (−0.5 V) occurs when the H*:NO_x* coverage ratio is optimized for selective NO_3^- reduction.[41] This potential appears more negative for Ni_2P than previously measured for Cu and Ni foils,[41] suggesting that Ni_2P can suppress HER over a wider potential window. We propose that Ni_2P's active site ensembles enable more optimal relative binding of H* and NO_x*, which is reflected by the shift in the potential of maximum rate order to more cathodic potentials. We also observe a decreasing NO_3^- rate order in the phosphate-mediated region (>−0.25 V) as we move to more negative potentials. We attribute this decrease to the rate being limited by $H_2PO_4^-$ ([H^+] or coverage of H*) instead of NO_3^-, which is supported by the presence of the $H_2PO_4^-$ deprotonation peak in Fig. 2a. This rate order analysis assumes that the rate of NO_3RR and HER are independent; however, assuming they are dependent results in identical conclusions (Fig. S9, ESI†).

The rate order analysis supports our hypothesis that Ni_2P/C can simultaneously co-adsorb multiple intermediates required to reduce NO_3^- to NH_3. To investigate how this influences the selectivity of NO_3RR, we conducted chronoamperometry experiments and quantified the products (Fig. 2c and Fig. S9, S10a, ESI†). NH_3 and NO_2^- were quantified with previously reported UV-visible colorimetric methods (Fig. S1 and S2, see ESI†). After considering three possible reaction pathways for NO_3RR to ammonia,[15,44] DFT calculations suggest that NH_3 is formed by an $8e^-$ sequential deoxygenation and hydrogenation pathway with a NO_2^- intermediate (Fig. S13 and S14, ESI†). *In situ* mass spectrometry measurements confirmed that the sole gaseous product is H_2 at −0.6 V from the competing HER (Fig. S11, ESI†). We believe H_2 is the sole gaseous product over the entire range of potentials due to the lack of N_2 and N_2O (which should have more sluggish kinetics than the other thermodynamically accessible products) at the most cathodic potential in the series. Bulk electrolysis results reveal that Ni_2P/C has >60% faradaic efficiency (FE) toward NO_3RR at all tested potentials and nearly 100% FE at −0.4 V. As potential decreases, NH_3 selectivity decreases and the production of H_2 and NO_2^- increases. We

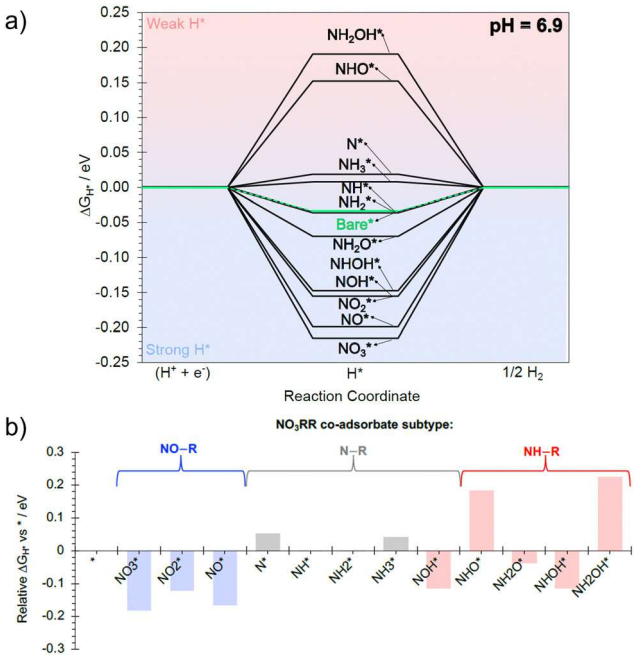

Fig. 3 (a) Calculated free energy profile at 0.00 V *vs.* RHE, pH = 6.9, and 300 K for the adsorption of H* onto the Ni_3 hollow site of the Ni_3P_2 terminated surface, with and without surface functional groups. (b) Plot showing the relative hydrogen adsorption free energy as a function of co-adsorbed species relative to ΔG_{H^*} on the bare Ni_2P surface (*), at pH = 6.9 and T = 300 K. The colors correspond to the co-adsorbate subtypes consisting of NO–R (blue), N–R (grey) and NH–R (red) containing species.

propose that the reaction selectivity is dictated by the ratio of H* and NO_x* on the surface, which is tuned by the applied potential. At low cathodic potentials (≥ -0.2 V) where NO_3^- reduction is mediated by $H_2PO_4^-$, we observe >80% NH_3 FE and 15–20% H_2 FE, with minimal NO_2^- production. We propose that the diffusion-limited nature of $H_2PO_4^-$ allows NO_x* to saturate the surface and decreases the ratio of H*:NO_x*. This coverage ratio favors the hydrogenation of NO_x* species to NH_3 over the formation of NO_2^- and H_2.[45,46] In the H_2O-mediated region (≤ -0.3 V), we observe near 100% FE toward NO_3RR at -0.4 V, which suggests a surface coverage that almost completely inhibits HER activity, *i.e.*, an ideal ratio of H*:NO_x* for selectively performing NO_3RR. Deviation from the ideal H*:NO_x* ratio results in lower NO_3RR selectivity. At -0.3V, we observe a rise in NO_2^- selectivity relative to -0.2 V due to H*:NO_x* being too low. Conversely, as potentials become more cathodic of -0.4 V, the H*:NO_x* ratio increases and favors H_2 formation by promoting H–H coupling over NO_x* hydrogenation, decreasing overall NO_3RR selectivity.

Complementary to the experiments, we also performed DFT calculations on a Ni_2P surface to disentangle the influence of NO_x* and H* co-adsorption on their respective energetics and reaction selectivity. Systematic exploration of various nitrogenous species reveals that co-adsorption of nitrogenous species and H* modulates ΔG_{H^*}, the key binding mode of nitrogenous species, and the overall free energy profile of the reaction (Fig. 3 and Fig. S14b, S15, see ESI†), which is consistent with previous work.[47] ΔG_{H^*} can be modulated by as much as 0.040 eV, where oxygenated, unhydrogenated nitrogenous species (*i.e.*, NO_3*, NO_2*) strengthen ΔG_{H^*}.

We hypothesize that stronger values of ΔG_{H^*} may direct Ni_2P/C's selectivity toward NH_3 even at negative reductive potentials (*i.e.*, -0.6 V). At these potentials, despite a strong driving force toward HER, NO_x* intermediates could be strengthening the adsorption of H*, which inhibits the Tafel step of HER and promotes the hydrogenation of NO_x*.[45,46] In general, the observed difference in ΔG due to co-adsorbed H* can be rationalized in terms of the electron-donating/withdrawing propensity and steric effects of the co-adsorbates, where in our system, the H* on a Ni_3-hollow site exhibits electrostatic repulsion effect on species such as NO_3^- and NO_2^-.[32,48,49] The impacts of H* and NO_x* on each other's surface energetics imply that the rates of NO_3RR and HER are inherently dependent, corroborating our conclusions from the rate-order analysis that NO_x* and H* are co-adsorbing on Ni_2P/C's active site ensembles during NO_3RR.

This work demonstrates Ni_2P/C's activity and selectivity for NO_3RR at a range of potentials, where NO_3RR FE is nearly 100% at -0.4 V and NH_3 selectivity is maximized in the $H_2PO_4^-$-mediated region. DFT calculations and rate order analysis demonstrate Ni_2P/C's ability to co-adsorb nitrogenous and hydrogen intermediates and selectively produce NH_3 over the range of potentials. We rationalize the potential-dependent selectivity of Ni_2P/C by changes in the surface coverage of adsorbates, where the ratio of H*:NO_x* at -0.4 V is ideal for performing NO_3RR over HER. This work is a case study of the importance of the active site ensembles on metal phosphide surfaces that drive nitrate reduction selectivity toward NH_3. This motivates future work in the design of metal phosphide electrocatalysts by controlling stoichiometry, doping, and morphology to tune catalytic activity.

E. N. and P. S. R. acknowledge funding from the Center for Molecular Electrocatalysis, an Energy Frontier Research Center funded by the U.S. Department of Energy, Office of Basic Energy Sciences. E. M. S., A. P., and B. R. acknowledge funding from the National Science Foundation (CBET 205227). Computational resources were provided by the National Energy Research Computing Center at LBNL. PNNL is operated by Battelle under contract number DEAC05-75RL01830.

Conflicts of interest

There are no conflicts to declare.

Notes and references

1 D. Baker, T. Brown, N. Cook, S. Cowley, S. Crolius, C. L. Smith, J. Makepeace, C. Philibert, A. Valera-Medina, I. Wilkinson and T. Wood, *Ammonia: zero-carbon fertiliser, fuel and energy store*, The Royal Society, 2020, pp. 1–40.
2 N. Gruber and J. N. Galloway, *Nature*, 2008, **451**, 293–296.
3 Y. Zeng, C. Priest, G. Wang and G. Wu, *Small Methods*, 2020, **4**, 2000672.
4 P. H. van Langevelde, I. Katsounaros and M. T. M. Koper, *Joule*, 2021, **5**, 290–294.

5 J. Li, G. Zhan, J. Yang, F. Quan, C. Mao, Y. Liu, B. Wang, F. Lei, L. Li, A. W. M. Chan, L. Xu, Y. Shi, Y. Du, W. Hao, P. K. Wong, J. Wang, S.-X. Dou, L. Zhang and J. C. Yu, *J. Am. Chem. Soc.*, 2020, **142**, 7036–7046.
6 T. Chen, H. Li, H. Ma and M. T. M. Koper, *Langmuir*, 2015, **31**, 3277–3281.
7 K. Chen, J. Xiang, Y. Guo, X. Liu, X. Li and K. Chu, *Nano Lett.*, 2024, **24**, 541–548.
8 Q. Hu, K. Yang, O. Peng, M. Li, L. Ma, S. Huang, Y. Du, Z.-X. Xu, Q. Wang, Z. Chen, M. Yang and K. P. Loh, *J. Am. Chem. Soc.*, 2024, **146**, 668–676.
9 J.-Q. Chen, X.-X. Ye, D. Zhou and Y.-X. Chen, *J. Phys. Chem. C*, 2023, **127**, 2918–2928.
10 H. Yin, F. Dong, Y. Wang, H. Su, X. Li, Y. Peng, H. Duan and J. Li, *Nano Lett.*, 2023, **23**, 11899–11906.
11 H. Yin, F. Dong, H. Su, Z. Zhuang, Y. Wang, D. Wang, Y. Peng and J. Li, *ACS Nano*, 2023, **17**, 25614–25624.
12 E. Murphy, Y. Liu, I. Matanovic, M. Rüscher, Y. Huang, A. Ly, S. Guo, W. Zang, X. Yan, A. Martini, J. Timoshenko, B. R. Cuenya, I. V. Zenyuk, X. Pan, E. D. Spoerke and P. Atanassov, *Nat. Commun.*, 2023, **14**, 4554.
13 Z.-Y. Wu, M. Karamad, X. Yong, Q. Huang, D. A. Cullen, P. Zhu, C. Xia, Q. Xiao, M. Shakouri, F.-Y. Chen, J. Y. (Timothy) Kim, Y. Xia, K. Heck, Y. Hu, M. S. Wong, Q. Li, I. Gates, S. Siahrostami and H. Wang, *Nat. Commun.*, 2021, **12**, 2870.
14 J.-X. Liu, D. Richards, N. Singh and B. R. Goldsmith, *ACS Catal.*, 2019, **9**, 7052–7064.
15 T. Hu, C. Wang, M. Wang, C. M. Li and C. Guo, *ACS Catal.*, 2021, **11**, 14417–14427.
16 X. Lu, H. Song, J. Cai and S. Lu, *Electrochem. Commun.*, 2021, **129**, 107094.
17 J. Ni, J. Yan, F. Li, H. Qi, Q. Xu, C. Su, L. Sun, H. Sun, J. Ding and B. Liu, *Adv. Energy Mater.*, 2024, 2400065.
18 Q. Liu, Y. Lin, S. Gu, Z. Cheng, L. Xie, S. Sun, L. Zhang, Y. Luo, A. A. Alshehri, M. S. Hamdy, Q. Kong, J. Wang and X. Sun, *Nano Res.*, 2022, **15**, 7134–7138.
19 G. Wang, Y. Zhang, K. Chen, Y. Guo and K. Chu, *Inorg. Chem.*, 2023, **62**, 6570–6575.
20 Q. Yao, J. Chen, S. Xiao, Y. Zhang and X. Zhou, *ACS Appl. Mater. Interfaces*, 2021, **13**, 30458–30467.
21 Q.-L. Hong, J. Zhou, Q.-G. Zhai, Y.-C. Jiang, M.-C. Hu, X. Xiao, S.-N. Li and Y. Chen, *Chem. Commun.*, 2021, **57**, 11621–11624.
22 Y. Jia, Y.-G. Ji, Q. Xue, F.-M. Li, G.-T. Zhao, P.-J. Jin, S.-N. Li and Y. Chen, *ACS Appl. Mater. Interfaces*, 2021, **13**, 45521–45527.
23 R. Zhang, Y. Guo, S. Zhang, D. Chen, Y. Zhao, Z. Huang, L. Ma, P. Li, Q. Yang, G. Liang and C. Zhi, *Adv. Energy Mater.*, 2022, **12**, 2103872.
24 S. Huo, S. Yang, Q. Niu, Z. Song, F. Yang and L. Song, *ChemCatChem*, 2020, **12**, 4600–4610.
25 L. Wen, Y. Sun, C. Zhang, J. Yu, X. Li, X. Lyu, W. Cai and Y. Li, *ACS Appl. Energy Mater.*, 2018, **1**, 3835–3842.
26 B. Liu, X. Lan, Q. Zhong and T. Wang, *ACS Catal.*, 2024, **14**, 757–775.
27 D.-Y. Kuo, E. Nishiwaki, R. A. Rivera-Maldonado and B. M. Cossairt, *ACS Catal.*, 2023, **13**, 287–295.
28 P. Liu and J. A. Rodriguez, *J. Am. Chem. Soc.*, 2005, **127**, 14871–14878.
29 E. J. Popczun, J. R. McKone, C. G. Read, A. J. Biacchi, A. M. Wiltrout, N. S. Lewis and R. E. Schaak, *J. Am. Chem. Soc.*, 2013, **135**, 9267–9270.
30 B. Seo, D. San Baek, Y. Jin Sa and S. Hoon Joo, *CrystEngComm*, 2016, **18**, 6083–6089.
31 C. A. Downes, K. M. Van Allsburg, S. A. Tacey, K. A. Unocic, F. G. Baddour, D. A. Ruddy, N. J. LiBretto, M. M. O'Connor, C. A. Farberow, J. A. Schaidle and S. E. Habas, *Chem. Mater.*, 2022, **34**, 6255–6267.
32 I. A. Murphy, P. S. Rice, M. Monahan, L. P. Zasada, E. M. Miller, S. Raugei and B. M. Cossairt, *Chem. Mater.*, 2021, **33**, 9652–9665.
33 S. Banerjee, A. Kakekhani, R. B. Wexler and A. M. Rappe, *ACS Catal.*, 2021, **11**, 11706–11715.
34 K. U. D. Calvinho, A. W. Alherz, K. M. K. Yap, A. B. Laursen, S. Hwang, Z. J. L. Bare, Z. Clifford, C. B. Musgrave and G. C. Dismukes, *J. Am. Chem. Soc.*, 2021, **143**, 21275–21285.
35 K. U. D. Calvinho, A. B. Laursen, K. M. K. Yap, T. A. Goetjen, S. Hwang, N. Murali, B. Mejia-Sosa, A. Lubarski, K. M. Teeluck, E. S. Hall, E. Garfunkel, M. Greenblatt and G. C. Dismukes, *Energy Environ. Sci.*, 2018, **11**, 2550–2559.
36 M. S. Duyar, A. Gallo, S. K. Regli, J. L. Snider, J. A. Singh, E. Valle, J. McEnaney, S. F. Bent, M. Rønning and T. F. Jaramillo, *Catalysts*, 2021, **11**, 143.
37 C. A. Downes, N. J. Libretto, A. E. Harman-Ware, R. M. Happs, D. A. Ruddy, F. G. Baddour, J. R. Ferrell III, S. E. Habas and J. A. Schaidle, *ACS Appl. Energy Mater.*, 2020, **3**, 10435–10446.
38 L. Wei, D.-J. Liu, B. A. Rosales, J. W. Evans and J. Vela, *ACS Catal.*, 2020, **10**, 3618–3628.
39 M. E. Mundy, D. Ung, N. L. Lai, E. P. Jahrman, G. T. Seidler and B. M. Cossairt, *Chem. Mater.*, 2018, **30**, 5373–5379.
40 F. G. Baddour, E. J. Roberts, A. T. To, L. Wang, S. E. Habas, D. A. Ruddy, N. M. Bedford, J. Wright, C. P. Nash, J. A. Schaidle, R. L. Brutchey and N. Malmstadt, *J. Am. Chem. Soc.*, 2020, **142**, 1010–1019.
41 O. Q. Carvalho, R. Marks, H. K. K. Nguyen, M. E. Vitale-Sullivan, S. C. Martinez, L. Árnadóttir and K. A. Stoerzinger, *J. Am. Chem. Soc.*, 2022, **144**, 14809–14818.
42 N. Singh, U. Sanyal, G. Ruehl, K. A. Stoerzinger, O. Y. Gutiérrez, D. M. Camaioni, J. L. Fulton, J. A. Lercher and C. T. Campbell, *J. Catal.*, 2020, **382**, 372–384.
43 Z. Wang, D. Richards and N. Singh, *Catal. Sci. Technol.*, 2021, **11**, 705–725.
44 Y. Cao, S. Yuan, L. Meng, Y. Wang, Y. Hai, S. Su, W. Ding, Z. Liu, X. Li and M. Luo, *ACS Sustainable Chem. Eng.*, 2023, **11**, 7965–7985.
45 K. Yang, S.-H. Han, C. Cheng, C. Guo, T. Li and Y. Yu, *J. Am. Chem. Soc.*, 2024, **146**, 12976–12983.
46 Y. Xiong, Y. Wang, J. Zhou, F. Liu, F. Hao and Z. Fan, *Adv. Mater.*, 2024, **36**, 2304021.
47 H. Yuan, N. Sun, J. Chen, J. Jin, H. Wang and P. Hu, *ACS Catal.*, 2018, **8**, 9269–9279.
48 P. S. Rice, Y. Mao, C. Guo and P. Hu, *Phys. Chem. Chem. Phys.*, 2019, **21**, 5932–5940.
49 P. S. Rice, Z.-P. Liu and P. Hu, *J. Phys. Chem. Lett.*, 2021, **12**, 10637–10645.

